
An MCMC-Based Analysis of a Multilevel Model for Functional MRI Data

Brian Caffo, DuBois Bowman, Lynn Eberly, and Susan Spear Bassett

14.1 Introduction

Functional neuroimaging technologies have inspired a revolution in the study of brain function and its correlation with behavior, disease, and environment. In these techniques, temporal three-dimensional images of the brain are analyzed to produce a quantitative description of brain function. Such techniques can, among other things, present evidence of localization of brain function within and between subjects. For example, when subjects perform motor tasks in a functional magnetic resonance imaging (fMRI) scanner, such as finger tapping, the analysis typically will present increased regional cerebral blood flow (activation) in the motor cortex. Moreover, these techniques can also provide some information about how areas of the brain connect and communicate. In this chapter we further investigate a novel Markov chain Monte Carlo (MCMC) based analysis of a model from Bowman et al. (2008) that combines activation studies with the study of brain connectivity in a single unified approach.

This idea of localization of brain function underlying fMRI activation studies has a long history, with early attempts from the debunked science of phrenology in the early nineteenth century and later breakthroughs by such luminaries as Broca, Wernicke, and Brodman (see Gazzaniga et al., 2002, for an accessible brief history). Prior to new measurement techniques, studies of brain function and localization were limited to animal studies, or post-mortem evaluation of patients with stroke damage or injuries. However, new measurement techniques, such as fMRI, positron emission tomography (PET), and electroencephalography, allow modern researchers noninvasively to study brain function in human subjects.

In contrast with the study of functional localization, the companion idea of connectivity has a shorter history. Functional connectivity is defined as correlation between remote neurophysiological events (Friston et al., 2007). This idea is based on the principal of functional integration of geographically separated areas of the brain. Such integration is supported by the existence of anatomical connections between cortical areas as well as ones within the cortical sheet (see the discussion in Friston et al., 2007). This neuroanatomical model suggests a hierarchical structure of connectivity that includes correlations within and between areas of functional specialization. Therefore, we use this hierarchical biological model of brain function to explore a multilevel statistical model that simultaneously considers potentially long-range correlations as well as shorter-range ones.

We focus on analyzing fMRI data in particular, though the statistical and computational techniques apply more broadly to other functional neuroimaging modalities. Functional

MRI has its roots in the late nineteenth-century discovery that neuronal activity was accompanied by a localized increase in blood flow (Roy and Sherrington, 1890). More specifically, neuronal activity requires energy, which is supplied by chemical reactions from oxygenated hemoglobin. Therefore, provided a cognitive task is localized, a temporal comparison of blood oxygenation levels when the task is being executed versus when it is not would reveal areas of the brain where neurons are active. This is the principle of blood oxygenation level dependent (BOLD) fMRI (Ogawa et al., 1990). In this technique, a subject in an MRI scanner is asked to perform a task at specific timings while images targeting the BOLD signal are taken in rapid succession, usually one image every 2–3 seconds. Examples of tasks are motor tasks, pressing a button after a visual stimulus, mentally rotating figures and so on. The development of a well-controlled task, or paradigm, that isolates the particular cognitive function of interest is not covered in this chapter.

We focus on using Bayesian multilevel models via MCMC for the analysis of functional neuroimaging studies. We emphasize the analysis of so-called group-level fMRI data. In such studies one is interested in the commonality of activation and connectivity within groups and differences between groups, such as comparing diseased and control subjects.

In the following two subsections, we provide an overview of existing related fMRI research and introduce the data used to illustrate the methods. In Section 14.2, we give details on the processing and first-stage analysis of the data. In Section 14.3, we introduce the multilevel model used for analysis and outline the details of the MCMC procedure. In Section 14.4, we propose novel methods for analyzing and visualizing the output from the Markov chain, including the analysis of voxel means, regional means, and intra- and inter-regional connectivity. We conclude with a discussion.

14.1.1 Literature Review

Traditional inter-group analyses of fMRI data employ a two-stage procedure, where a first stage relates the paradigm to the images and a second stage compares contrast estimates from the first stage across subjects groups. This two-stage process is motivated by classical two-stage procedures for linear mixed effects models (see Verbeke and Molenberghs, 2000) and has the benefit of greatly reducing the amount of data to be considered in the second stage. Two-stage analysis of fMRI is proposed and considered in Beckmann et al. (2003), Friston et al. (1999, 2005), and Holmes and Friston (1998), among others. See also Worsley et al. (2002) for a more formal discussion of two-stage random effects approaches for fMRI data.

Standard methods for analyzing two-stage data ignore spatial dependence and connectivity at the modeling level and instead incorporate the spatial dependence into the analysis of statistical maps created from the models. The map of statistics is assumed to possess a conditionally independent neighborhood structure, typically a Markov random field. Further descriptions of the use of Markov random fields in neuroimaging analysis can be found in Worsley (1994), Cao and Worsley (2001), Worsley and Friston (1995), Worsley et al. (1996), and Friston et al. (2007). These approaches are notable for their speed and general applicability. However, they are also characterized by several issues of concern. First, the random field assumptions are somewhat restrictive, as they do not allow for long-range functional correlations and impose a rigid distributional structure. Moreover, many desirable summary statistics have unknown distributions when the statistical map follows a random field. Therefore, indirect inference is typically used by considering a fairly narrow class of statistics with tractable distributions. Conceptually, this could be combated via simulation from

the random field under the null hypothesis. However, a more popular approach uses resampling methods, mostly focused on permutation testing. At the expense of computational complexity, these methods can flexibly handle any test statistic, and make few assumptions on the underlying distribution and correlation structure of the data. Permutation methods, as applied to neuroimaging data, are reviewed in Nichols and Holmes (2002). An example for factorial experiments is given in Suckling and Bullmore (2004). Comparisons between cluster-size permutation tests and random-field intensity tests are given in Hayasaka and Nichols (2003). Despite their numerous benefits, permutation methods are focused on testing and do not offer generative models for the data. That is, unlike model-based methods, permutation testing lacks a formal mechanism for connecting the data to a population.

Multilevel models for inter-group analysis of fMRI data have become increasingly popular. Bowman et al. (2008) gave a Bayesian approach and applied it to both Alzheimer's disease and substance abuse disorder data sets; the model from that article motivates the analysis in this chapter. Bowman and Kilts (2003) give a multilevel model applied to the related area of functional PET imaging. The theory and application of Bayesian models is discussed in Friston et al. (2002a,b). Woolrich et al. (2004) use reference priors for inter-group Bayesian fMRI analysis.

Functional MRI connectivity studies have largely focused on the analysis of resting state data, based on the hypothesis of a default-mode brain network (Biswal et al., 1995; Greicius, 2003). These networks represent functional correlations in brain activity between voxels while resting in the scanner. Xiong et al. (1999) considered such resting-state connectivity between regions and compared results to those motivated by other techniques. Greicius (2004) used independent component analysis to explore resting state connectivity (see Calhoun et al., 2003). Arfanakis et al. (2000) considered connectivity via regional correlations and independent components analysis. However, unlike the previous references, they considered active-state data collected along with an experimental fMRI paradigm, though focused on connectivity results in areas unassociated with the paradigm. Our approach differs drastically from these references, both in terms of the methodology considered and the goal. With regard to methodology, we consider a model-based approach to connectivity and decompose connectivity into both short-range connections and longer-range connections. Moreover, our focus is on connectivity associated with a paradigm, and how this connectivity varies across experimental groups. That is, we consider areas of the brain that act in concert to perform the paradigm, rather than considering a default-mode brain network.

14.1.2 Example Data

The data used in our examples come from a study of subjects at high familial risk for Alzheimer's disease and controls with little familial risk. Alzheimer's disease is a degenerative memory disorder affecting millions of adults in the United States alone (Brookmeyer et al., 1998). Typically, Alzheimer's disease affects adults older than 65 years, though early onset cases do occur. The disease causes dementia, with the most common early symptom being short-term memory loss. Because precursors of the disease, such as mild cognitive impairment, occur well before clinical diagnoses, the study of at-risk individuals yields important information about early disease pathology (Bassett et al., 2006; Fox et al., 2001). Because some of the at-risk subjects will not become eventual cases, and some of the controls may become cases, larger sample sizes are necessary for a prospective or cross-sectional study of familial risk. In this study, the at-risk subjects had at least one parent with autopsy-confirmed Alzheimer's disease and at least one additional affected first-degree relative as per a clinical diagnosis of probable Alzheimer's disease. However, the subjects themselves

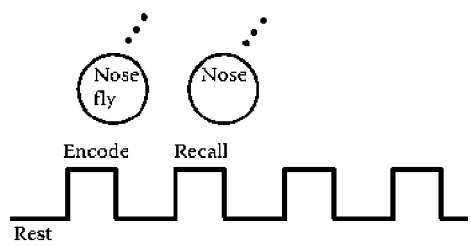


FIGURE 14.1
Illustration of the paradigm.

had no clinical Alzheimer’s disease symptoms. Control subjects were also asymptomatic and had no affected first-degree relatives. The study is impressive in its scope, with over 80 subjects in each group, which is atypically large for an fMRI study.

The fMRI paradigm, an auditory word-pair-associate task developed by Bookheimer et al. (2000), was chosen because its primary locus of activation is in the medial temporal lobe, a site of early neuropathological changes associated with Alzheimer’s disease. Moreover, loss of verbal memory is an important component of Alzheimer’s disease symptoms (Martin et al., 1985). The task consisted of encoding and recall blocks, where subjects heard an unrelated pair of words in the encoding phase and were asked to remember the second word when prompted with the first in the recall phase. The paradigm included two six-minute sessions, each consisting of seven unique word-pairs. A pictorial description of the task is given in Figure 14.1, while further technical information is given in Bassett et al. (2006). A sagittal profile of the image acquisition area for a specific subject is given in Figure 14.2.

Known anatomically-derived (Tzourio-Mazoyer et al., 2002) regions of interest (ROIs) are overlaid onto the single-subject maps. This parcelation allows for the study of inter- and intra-regional connectivity. Only those voxels in the image acquisition area with a substantial (greater than 10 voxels) intersection with an ROI are retained. Specifically, let v be a voxel, I be the collection of voxels in the image acquisition area and ROI_i be the collection of voxels in region of interest i . Voxel v is retained if $v \in ROI_i$ for some i and $I \cap ROI_i$ contains more than 10 voxels. This drastically reduces the number of voxels under



FIGURE 14.2
Image acquisition area (darker gray region) overlaid on template brain. The image is displayed such that anterior is to the right and posterior to the left. The superior portion has been cropped to display an axial slice. (See online supplement for color figures.)

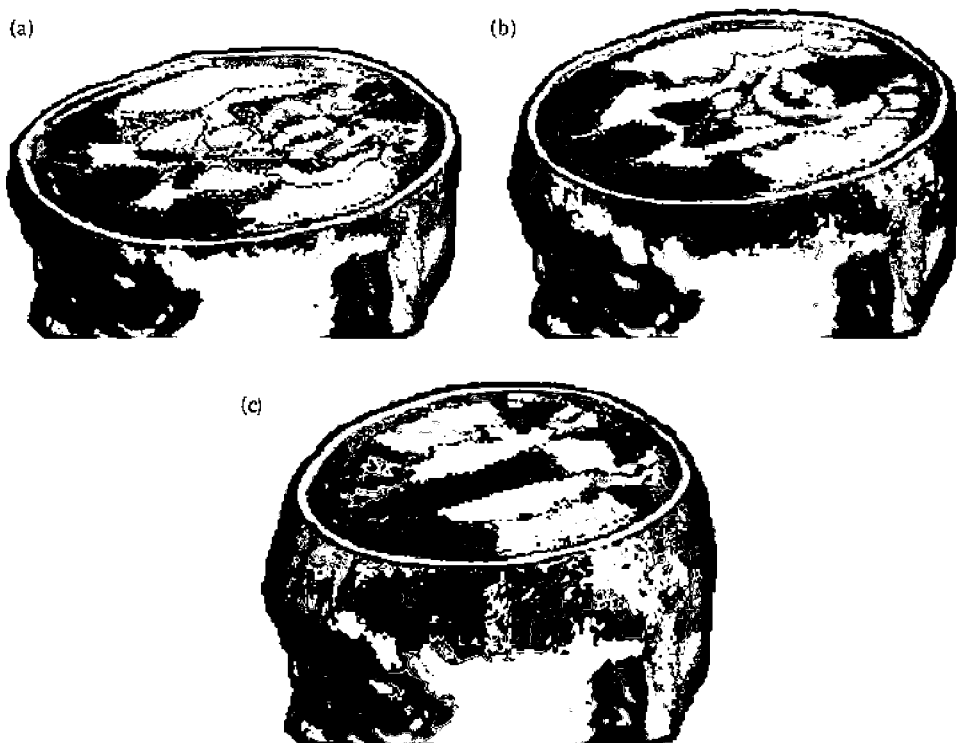


FIGURE 14.3
Example region of interest definitions for three axial slices. Each shade of gray represents a different region. (See online supplement for color figures.)

consideration and further limits the imaging area available for study. Figure 14.3 depicts the ROI definitions for three axial slices.

14.2 Data Preprocessing and First-Level Analysis

Following Friston et al. (2005), Holmes and Friston (1998), and others, we approach our analysis using a two-stage procedure. In the first stage, the data are preprocessed and contrast estimates obtained by linear regression over the time series, such as those comparing active states to rest, are retained for a second-stage analysis. The results is an image of contrast estimates, one per subject, that are then compared across subjects. This approach approximates random effect modeling and has several notable benefits. A principal one, however, is the issue of data reduction, as the contrast maps retained for the second stage are much smaller than the raw fMRI time series of images. However, we emphasize that this approach can have limiting assumptions, such as the inability to incorporate within-session temporal effects into group-level analyses. Such criticisms can be addressed by retaining some of the within-session temporal information for the second stage, such as by fitting separate effects for each block of the paradigm and analyzing them jointly in the second-stage analysis (Bowman and Kilts, 2003). However, this strategy results in less data reduction for

the second stage. Hence, in this chapter, we perform a second-stage analysis using only the contrast maps from the first while stipulating this potential limiting assumption.

Our preprocessing strategy was similar to those discussed in Friston et al. (1995, 2007) and Frackowiak et al. (2004). First, the within-subject images were spatially renormalized to the first image via rigid-body transformations. Secondly, these images were transformed into Montreal Neurological Institute (MNI) template space, so that valid comparisons could be made across subjects. Contrary to standard practice, we did not then smooth the images, as the second-stage model contains random effects that shrink voxel-level means within regions.

Next, a canonical hemodynamic response function (HRF) was convolved with indicator functions for the task sequence. This step is necessary as the BOLD signal is only a proxy for neuronal activity. In fact, initially after the onset of the task, blood oxygenation levels will be slightly decreased before being replenished. Therefore, task-related increases in the BOLD signal are expected after a short lag subsequent to the onset of the task. The use of a canonical HRF is another somewhat limiting assumption for this and many other studies, as it varies both across subjects and spatially within subjects due to, among other processes, kinetics of the vasculature.

Let $y_i(v) = \{y_{i1}(v), \dots, y_{iT}(v)\}^t$ be the temporal response vector for subject $i = 1, \dots, I$, voxel $v = 1, \dots, V$, and time index $t = 1, \dots, T$. Let X be a $T \times p$ matrix of an intercept and hemodynamically convolved indicator functions associated with the paradigm. Let H be a $T \times q$ design matrix of slowly varying trend terms, such as a linear trend and low frequency trigonometric terms, to serve as a high-pass filter. This can account for slowly varying systematic effects, such as scanner drift, where the signal can steadily increase or decrease over a session. Then the general linear model fit for subject i at voxel v is given by

$$y_i(v) = X\beta_i(v) + H\gamma_i(v) + \epsilon_i(v), \quad (14.1)$$

where $\epsilon_i(v) = \{\epsilon_{i1}(v), \dots, \epsilon_{iT}(v)\}^t$ are assumed to be an AR(1) process, $\text{corr}\{\epsilon_{it}(v), \epsilon_{i,t-k}(v)\} = \rho(v)^k$, with an innovation variance $\sigma^2(v)$. Our two-stage procedure retains a contrast estimate from Equation 14.1 for the inter-subject model considered in the next section. For example, we consider the comparison of encoding blocks versus rest, taking the contrast estimate at each voxel, hence creating a contrast map for each subject.

14.3 A Multilevel Model for Incorporating Regional Connectivity

14.3.1 Model

We consider decomposing the template brain into G regions, as depicted in Figure 14.3 (Tzourio-Mazoyer et al., 2002). As in Bowman et al. (2008), let $\hat{\beta}_{igj}(v)$ denote the contrast estimate from model (Equation 14.1) for subject $i = 1, \dots, I_j$ having condition $j = 1, \dots, J$, in region $g = 1 \dots G$ and voxel $v = 1, \dots, V_g$, where V_g is the number of voxels contained in region g . In our application $J = 2$, differentiating at-risk and control subjects, $G = 46$, $I_1 = 71$ and $I_2 = 83$. Throughout we adopt the convention that omitting the voxel-level parentheses refers to a vector over voxels, such as $\hat{\beta}_{igj} = \{\hat{\beta}_{igj}(1), \dots, \hat{\beta}_{igj}(V_g)\}^t$.

The multilevel model that we explore is the following:

$$\begin{aligned}
 \hat{\beta}_{igj}(v) \mid \mu_{gj}(v), \alpha_{igj}, \sigma_{gj}^{-2} &\sim N\{\mu_{gj}(v) + \alpha_{igj}, \sigma_{gj}^2\} \\
 \mu_{gj}(v) \mid \lambda_{gj}^2 &\sim N\{\mu_{0gj}, \lambda_{gj}^2\} \\
 \sigma_{gj}^{-2} &\sim \Gamma(a_0, b_0) \\
 \alpha_{ij} \mid \Gamma_j &\sim \text{MVN}(\mathbf{0}, \Gamma_j) \\
 \lambda_{gj}^{-2} &\sim \Gamma(c_0, d_0) \\
 \Gamma_j^{-1} &\sim \text{Wishart}\left\{ (l_0 H_0)^{-1}, l_0 \right\},
 \end{aligned} \tag{14.2}$$

where $\alpha_{ij} = (\alpha_{i1j}, \dots, \alpha_{iGj})'$. Here, $\mu_{gj}(v)$ is the mean contrast across subjects but within groups. The term α_{igj} represents subject- and region-specific deviations from the mean. This term forces a conditional exchangeable correlation structure within regions of $\rho_{gj} = \frac{\gamma_{gj}}{\gamma_{gj} + \sigma_{gj}^2}$, where γ_{gj} is diagonal element g from Γ_j . Thus, ρ_{gj} measures the correlation of contrast estimates within a region and group. We refer to it as a measure of *intra*-regional paradigm-related connectivity. In contrast, Γ_j is the variance-covariance matrix of the random effect terms between the G ROIs for condition j . Hence, we view the corresponding correlation matrix, say R_j , as a measure of *inter*-regional paradigm-related connectivity.

The residual variance, σ_{gj}^2 , is constant within regions, unlike many models for fMRI that presume separate voxel-specific variances. That is, instead of smoothing voxel-specific variances with further hierarchies, our model uses anatomical information to smooth variances within regions. Note that separate variances are assumed for each of the groups. The other variance term, λ_{gj} , measures variation in the voxel-level means around the prior mean, μ_{0gj} .

14.3.2 Simulating the Markov Chain

The block full conditionals associated with model (Equation 14.2) (see Bowman et al., 2008, for more discussion) are given below:

$$\begin{aligned}
 \mu_{gj} &\sim N\left[\left(\lambda_{gj}^{-2} + I_j \sigma_{gj}^{-2}\right) \left\{ \lambda_{gj}^{-2} \mu_{0gj} + I_j \sigma_{gj}^{-2} (\bar{\beta}_{gj} - \mathbf{1} \bar{\alpha}_{gj}) \right\}, \text{Diag}\left(\lambda_{gj}^{-2} + I_j \sigma_{gj}^{-2}\right)\right] \\
 \sigma_{gj}^{-2} &\sim \Gamma\left\{a_0 + I_j V_g/2, \left(\frac{1}{b_0} + \frac{1}{2} \sum_{i=1}^{I_j} \|\hat{\beta}_{igj} - \mu_{gj} - \mathbf{1} \alpha_{igj}\|^2\right)^{-1}\right\} \\
 \alpha_{ij} &\sim N\left[\left(\Gamma_j^{-1} + D_j^{-1}\right)^{-1} \left\{ D_j^{-1} (\bar{\beta}_{ij} - \bar{\mu}_j) \right\}, \left(\Gamma_j^{-1} + D_j^{-1}\right)\right] \\
 \lambda_{gj}^{-2} &\sim \Gamma\left\{c_0 + V_g/2, \left(\frac{1}{d_0} + \frac{(\mu_{gj} - \mu_{0gj})'(\mu_{gj} - \mu_{0gj})}{2}\right)^{-1}\right\} \\
 \Gamma_j^{-1} &\sim \text{Wishart}\left\{\left(l_0 H_0 + \sum_{i=1}^{I_j} \alpha_{ij} \alpha_{ij}'\right)^{-1}, l_0 + I_j\right\},
 \end{aligned} \tag{14.3}$$

where $\mu_{gj} = \{\mu_{gj}(1), \dots, \mu_{gj}(V_G)\}^t$, $\bar{\beta}_{gj}$ is $\frac{1}{I_j} \sum_{i=1}^{I_j} \{\hat{\beta}_{igj}(1), \dots, \hat{\beta}_{igj}(V_G)\}^t$, $\bar{\alpha}_{gj} = \frac{1}{I_j} \sum_{i=1}^{I_j} \alpha_{igj}$, $D_j = \text{Diag}(V_1 \sigma_{1j}^{-2}, \dots, V_G \sigma_{Gj}^{-2})$ and $\bar{\mu}_j = \left\{ \frac{1}{V_1} \sum_{v=1}^{V_1} \mu_{1j}(v), \dots, \frac{1}{V_G} \sum_{v=1}^{V_G} \mu_{Gj}(v) \right\}^t$. The update order proceeded with Γ_j first, then a loop over g for μ_{gj} , σ_{gj} , λ_{gj} , and then the update for α_{ij} .

The full conditionals display the benefit of the use of the linear mixed effects model and “Gibbs-friendly” prior distributions. That is, the full conditionals are based on simple matrix summaries that can be executed quickly. We discuss simple extensions with less restrictive priors in Section 14.6. Also note that none of the block updates have dimension larger than $\max_g V_g = 1784$ and, more importantly, no matrix inversions are required for matrices with dimension larger than $\max_g V_g \times \max_g V_g$. This is a primary strength of the model, as any approach that requires matrix manipulations over all of the voxels would not allow the fast block updates. The code was written in MATLAB® (Mathworks version 2006b) and is available from the first author’s website. Ten thousand iterations were run for the results presented; however, later runs of 100,000 iterations confirm the conclusions. Note that, with over 60,000 variables updated in each iteration (roughly 30,000 per group), this resulted in over 100 million basic operations. Regardless, the sampler was run on a standard laptop in under an hour (2.16 GHz dual core Intel processor and 2 GB of RAM).

With dimension in excess of 60,000, the posterior raises numerous issues regarding simulating the chain and analyzing the output. First, we note that storage of the output is itself a challenge. Memory allocation limits were reached if the entire chain of voxelwise results was stored for any reasonably long chain. We adopted the following strategy to combat this issue. The complete chain was stored for all of the values that have only tens of measurements per region. That is, the complete chain was stored for the σ_{gj} , α_{ij} , λ_{gj} , and Γ_j . For the μ_{gj} , the complete posterior mean was updated each iteration and stored. In addition, a batch means estimate (Jones et al., 2006) of the variance of this posterior mean was also stored. To utilize simple update rules, adaptive batch sizes were not employed and, instead, fixed batch sizes of size 100 were used. Moreover, the complete chains for several regional summaries, such as the mean and quantiles of the μ_{gj} within regions, were also stored. Finally, the complete value of μ_{gj} was stored for every 20th iteration, resulting in 500 total stored iterations. However, it should be noted that considerable loss of information is incurred if the chain is subsampled (MacEachern and Berliner, 1994). We do not recommend combining the values, subsampled or not, into a matrix or other single data structure. Instead, we recommend that the value for each saved iteration be stored in a separate file, with the filename indicating the iteration number.

For starting values, we used empirical moments and cumulants. Specifically, we let μ_{gj} be the empirical vector mean over the I_j subjects within region g and group j . We let σ_{gj}^2 be the average (across voxels) of the inter-subject variances within region g and group j . We let λ_{gj} be the between-region variance of the region- and group-specific means of the $\hat{\beta}_{igj}(v)$ ($\bar{\beta}_{gj}$ from above). We further let α_{igj} be the mean of the $\hat{\beta}_{igj}(v)$ within subject, region, and group. Then Γ_j was set to be the variance-covariance matrix of the starting value for α_{ij} , calculated by taking variances and covariances over subjects. The least accurate of these starting values are those for the α_{igj} and Γ_j , as the starting value for α_{igj} has mean $\frac{1}{V_g} \sum_{v=1}^{V_g} \mu_{gj}(v) + \alpha_{igj}$ (see Equation 14.2). However, recall that the outcomes are contrasts estimates and ideally the task should specialize to only a small portion of the brain, and therefore the term $\frac{1}{V_g} \sum_{v=1}^{V_g} \mu_{gj}(v)$ should be small in absolute value. Hence, for starting values, ignoring the fixed effects contribution in the moment estimates is not problematic.

To empirically evaluate the results of the chain, posterior mean estimates were compared with these starting values. In all cases they agreed well, though we stipulate that this only adds to the face validity of the chain and is not a formal method of convergence assessment. To further evaluate properties of the chain, trace plots of the parameters were investigated. However, the volume of parameters precludes investigation of all plots for the $\mu_{gj}(v)$. Instead, a random sample of voxels was selected and investigated in greater detail. To investigate sensitivity to hyperparameter settings, several chains were run, varying these parameters.

14.4 Analyzing the Chain

14.4.1 Activation Results

We consider the distribution of voxel-level contrast means to answer the question of whether the μ_{gj} are systematically larger than zero in any area and whether they differ across groups. The former question is of greater initial importance, as there is less interest in assessing inter-group differences when there is little evidence of localized within-group activation. We use a novel adaptation of a supra-threshold clustering technique widely used in the frequentist analysis of statistical maps. To evaluate a unit-free statistic, consider the map of voxel-level signal-to-noise statistics, $\{|\mu_{gj}(v)|/\sigma_{gj}\}_v$. Following traditional analysis, we consider clusters of contiguous connected voxels above a threshold (Cao and Worsley, 2001; Friston et al., 1993; Nichols and Holmes, 2002; Worsley, 1994; Worsley et al., 1996). Here, voxels are connected if they share a face, edge or corner. Figure 14.4 illustrates with fictitious one-dimensional data. We refer to the number of contiguous voxels in a cluster as the *extent*; in Figure 14.4 this is the width of the cluster above the chosen threshold. We also considered the center of mass of the cluster, the area of the cluster, and the peak value within the cluster. Here the center of mass is simply the average of the X , Y , and Z coordinates of each cluster surviving the threshold. The area of the cluster is proportional to taking the product of the voxels in the cluster and the associated heights of the statistics, and summing the results. Two cutoffs were considered for these supra-threshold statistics, 0.1 and 0.2. These were obtained empirically, by considering the inter-voxel distribution of the posterior means and

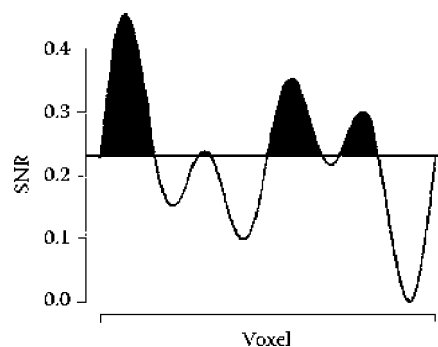


FIGURE 14.4
Illustration of supra-threshold cluster level statistics.

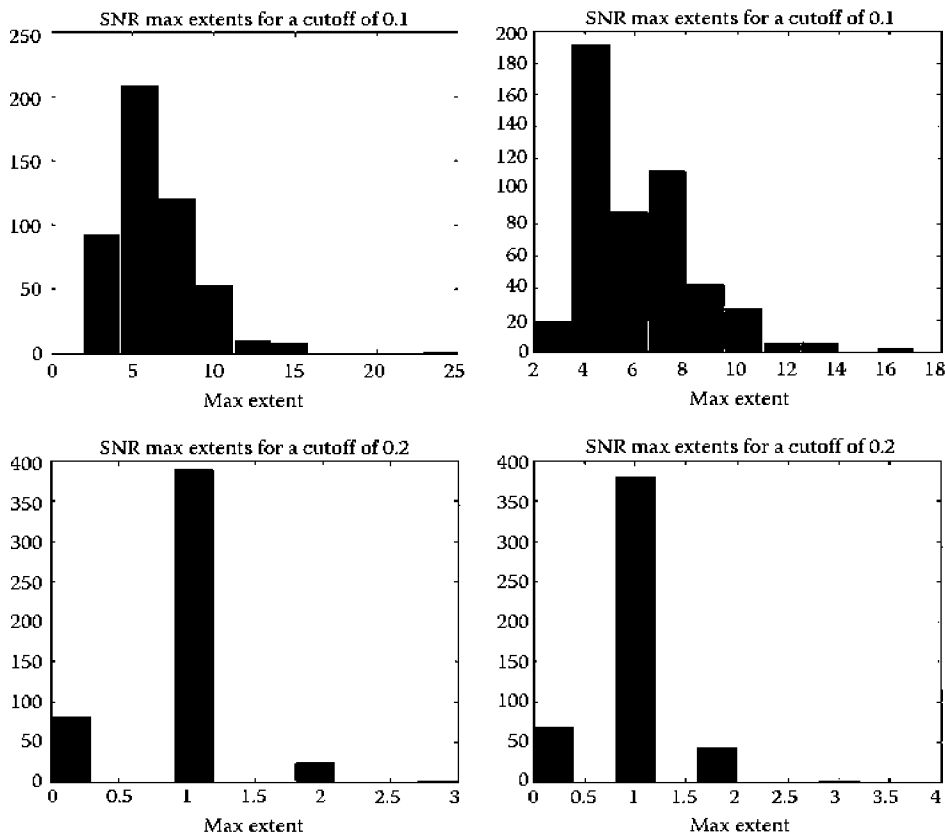
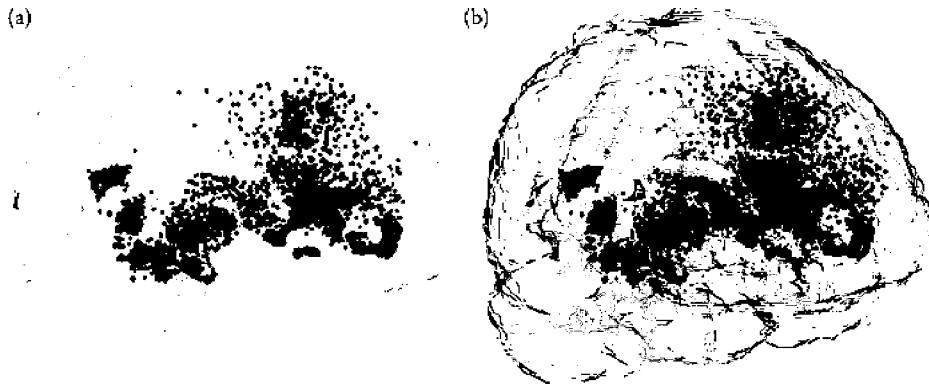


FIGURE 14.5

Estimated posterior distributions for the maximum supra-threshold cluster extents. The top and bottom images use an SNR cutoff of 0.1 and 0.2 respectively, and the left and right images correspond to at-risk and control groups respectively.

inspection of related data sets. Finally, to reduce cluster results to single numbers, we took the maximal statistic, such as considering the maximum cluster extent per MCMC iteration.

We considered thresholding the signal-to-noise statistic map generated at each MCMC iteration. As previously mentioned, a complication arose in that it is most convenient to have the chain of $\mu_{gj}(v)$ maps saved, as different thresholding values and statistics need to be evaluated interactively. As the complete chain is generally too large to save, we subsampled the chain and saved 500 equally spaced iterations. For each saved map, we determined the cluster size with the largest supra-threshold extent. Histogram estimates of the posterior distributions for the two groups and for the two cutoffs are given in Figure 14.5. Here the maximal extents appear to be quite small, suggesting little voxel-level activation across subjects within groups. Figure 14.6 displays the centroids for the clusters surviving the threshold (of 0.1) for the control group for the 500 saved iterations. The color and width of the points are related to the extent of the cluster. There is little evidence to suggest voxel-level localization of the clusters. In addition to considering the maximal extents, we also considered the areas under the clusters as well as the maximal peak value of the clusters. In each case, there was little suggestion of interesting voxel-level results. These conclusions are consistent with those of more standard analyses.

**FIGURE 14.6**

Plot of supra-threshold (threshold of 0.1) cluster centroids across 500 saved iterations for the control (a) and at-risk (b) groups. The shading and size of the points are proportional to the cluster extent. Transparent template brain overlays are provided for reference. (See online supplement for color figures.)

We also considered regional mean level effects. That is, let $\theta_{gj} = \sum_{v=1}^{V_g} \mu_{gj}(v) / V_g$, where V_g is the number of voxels in region g . As with the voxel-level results, we consider both within- and between-group effects. We first calculated the MCMC estimate of the minimum of the posterior tail probabilities of θ_{gj} being larger or smaller than 0, for each g and j :

$$\min\{P(\theta_{gj} < 0 \mid \text{Data}), P(\theta_{gj} > 0 \mid \text{Data})\}.$$

This quantity combines the information from the two one-sided tail probabilities similar to taking the smaller of two p -values from one-sided tests to perform a two-sided test. This is useful to answer whether or not the regional mean appears either much larger or smaller than zero.

In the control group, this quantity was the smallest in the right superior temporal lobe, with a posterior mean for θ_{gj} of -0.0021 and minimum tail probability of 0.0057. This was followed by the left supplementary motor area (0.0532) and the right mid frontal area (0.0586). In the at-risk group, there were only modestly small minimum tail probabilities in the left supplementary motor area (0.0560) and the right mid frontal area (0.0563).

To compare the two groups, we again evaluated a minimum of posterior tail probabilities. Specifically, we considered the minimum posterior probability of one mean being smaller or larger than the other. That is, for each g , we considered

$$\min\{P(\theta_{g1} < \theta_{g2} \mid \text{Data}), P(\theta_{g1} > \theta_{g2} \mid \text{Data})\},$$

where $j = 2$ refers to the at-risk group and $j = 1$ refers to the controls. This quantity was the smallest in the right superior temporal pole, with a minimum tail probability of 0.032, and in the right superior temporal lobe (0.0648). Histogram estimates of $\theta_{g1} - \theta_{g2}$ for these two regions are given in Figure 14.7, showing that activation related to this contrast is (largely speaking) slightly higher in the at-risk group compared to the controls.

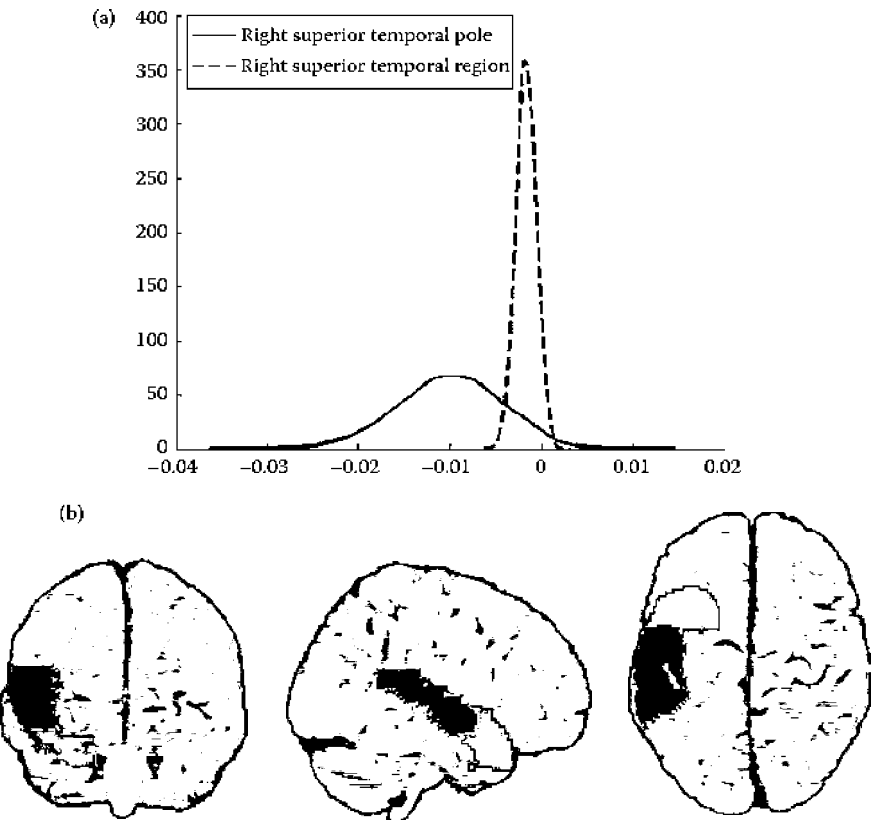


FIGURE 14.7 Posterior distributions for $\theta_{g1} - \theta_{g2}$ for the two regions with the smallest posterior tail probabilities. Projection plots of the two regions overlaid on a template brain are given for reference. (See online supplement for color figures.)

14.5 Connectivity Results

14.5.1 Intra-Regional Connectivity

We first consider results for intra-regional connectivity; that is, we consider the posterior distributions for the $\{\rho_{g_i}\}$. Figure 14.8 displays posterior credible intervals and posterior medians for the $\{\rho_{g_i}\}$ for the control and at-risk subjects for the 46 regions of interest, based on all 10,000 iterations. It is perhaps surprising that the correlations are as high as they are, especially given that no spatial smoothing was performed. We note that some of the variation in the intra-regional correlation arises from the size of the region in consideration, with, as expected, the smaller regions tending to demonstrate greater connectivity.

Figure 14.9 shows 95% equi-tail posterior credible intervals and posterior medians for the ratio ρ_1/ρ_2 , with a gray vertical reference line drawn at one. The data exhibit regions both with greater and lesser intra-regional connectivity. Figure 14.9 also displays projection maps of the regions with higher intra-regional connectivity among the controls (shown in the upper plots, as determined by a credible interval entirely above one) and lower intra-regional connectivity among the at risk (shown in the lower plots). Lower intra-regional

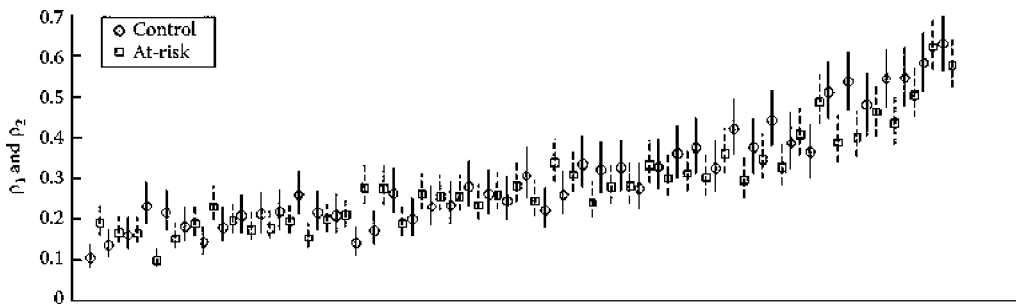


FIGURE 14.8

Posterior credible intervals and medians for ρ_1 (controls, circles) and ρ_2 (at-risk, squares). Intervals are ordered by the average of the two groups' medians.

connectivity among the control subjects was most apparent in the areas near the anterior cingulum. Higher intra-regional connectivity among the controls was most apparent in more frontal areas and was diffusely spread out.

14.5.2 Inter-Regional Connectivity

The proposed hierarchical model also allows for the study of inter-regional connectivity associated with the paradigm. Figure 14.10 connects the centroids of regions whose posterior mean correlation (from the off-diagonal entries of R_j) was above 0.6 for control (left) and at-risk (right) subjects, with estimates obtained using all 10,000 iterations. Visually, the picture suggests a denser network of connectivity for the at-risk subjects, perhaps suggesting that this population has to attend to the task more rigorously to complete it or that more regions are called upon to complete the task to compensate for weaknesses in a few regions. Below we explore more formal methods for comparing the chain of variance and covariance matrices. We consider the eigenvalue decomposition of the variance matrices, Γ_j , and the correlation matrices, R_j . This is analogous to a principal component analysis of the α_{ij} . In particular, we focus on the eigenvalue decomposition of the R_j , as the region-specific variances are of less interest.

The posterior mean of the percentage of variation explained by each component was 29, 13, 10, 8, and 6 for the control group and 29, 12, 9, 7, and 6 for the at-risk group. Figure 14.11 displays the posterior distribution for the largest eigenvalues for the control (solid) and at-risk subjects, respectively. We also looked at the distribution of the eigenvectors corresponding to the maximum eigenvalue. The at-risk group had larger loadings (across the board) for the first eigenvalue. The control group loaded most heavily (in absolute value) on the left precentral gyrus, the right mid cingulum, the right supplementary motor area, and the left postcentral gyrus. The at-risk group loaded more heavily on the left insula, the left precentral gyrus, the left caudate and left mid cingulum.

The equi-tail 95% posterior credible interval for the ratio of the largest eigenvalues (control over at-risk) was [0.58, 0.89], with a posterior distribution shown in the middle plot of Figure 14.11. To consider the variances, we considered the largest eigenvalue of $(\Gamma_1 + \Gamma_2)^{-1}\Gamma_1$, the greatest root statistic (Mardia et al., 1979). The equi-tail 95% credible interval for the greatest root statistic was [0.981, 0.989], with a posterior given in the rightmost plot of Figure 14.11.

Overall, the results suggest much greater connectivity in the at-risk group. We found this particular result to be the most intriguing for this data set and believe that it is suggestive of the idea that at-risk subjects have to engage more cognitive resources to attend to the task.

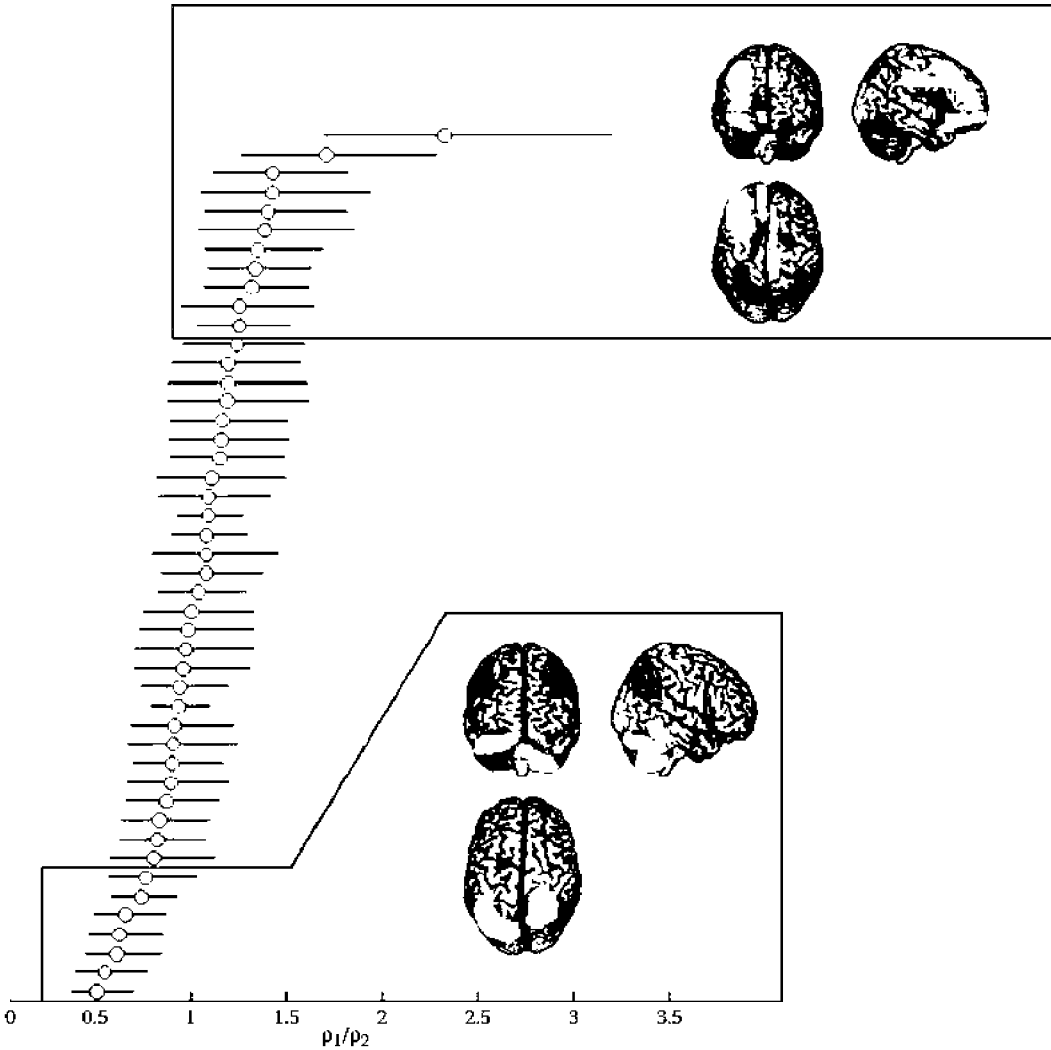
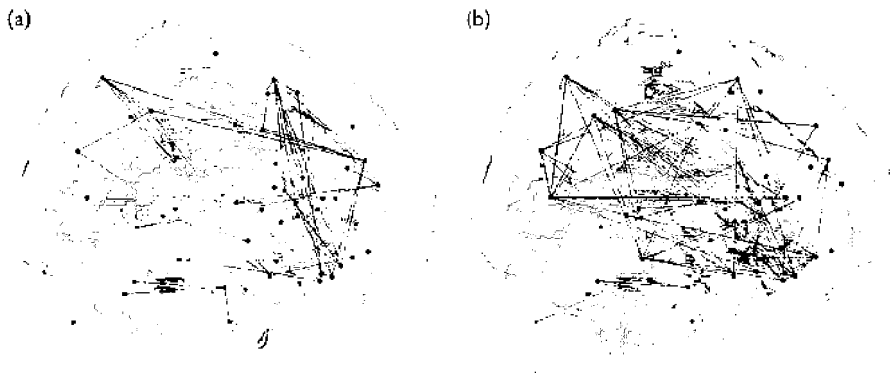


FIGURE 14.9 Credible intervals and posterior medians for ratios of ρ_1/ρ_2 accompanied by projection maps of the regions with credible intervals showing higher intra-regional connectivity among the at-risk (top plots, 11 regions) and higher connectivity among the controls (bottom plots, seven regions), respectively. Note that one of the top 11 and one of the bottom seven have credible intervals that overlap zero. (See online supplement for color figures.)

14.6 Discussion

In this chapter, we investigated a model from Bowman et al. (2008) and a data set from Bassett et al. (2006) and introduced some novel methods for analyzing, interpreting, and visualizing the output. The data are suggestive of some interesting findings on functional differences between a group of subjects at high risk for the development of Alzheimer’s disease and a group of controls. First, the voxel-level contrast map results suggest little difference between the groups in terms of activation, while the regional mean results suggest

**FIGURE 14.10**

Posterior mean connectivity estimates exceeding a threshold of 0.6 for control (a) and at-risk (b) subjects. Lines connect the centers of regions with posterior mean connectivity estimates exceeding the threshold. (See online supplement for color figures.)

a modest decrease in activation for the controls in two regions of the temporal lobe. These results, which have been confirmed with more traditional parametric modeling (not shown), differ from those of Bassett et al. (2006), based on the same subjects at an earlier visit. The discrepancy could be due to a variety of factors, such as a learning effect, differences in the sample (as there was dropout for the subsequent visit), or actual physiological longitudinal changes. We defer a full longitudinal analysis of this data to future research.

The connectivity results are perhaps more interesting in demonstrating greater differences between the two groups. The inter-regional results suggest greater connectivity among the at-risk groups. This result potentially suggests that the at-risk group are calling on greater cognitive reserves to perform the tasks. The intra-regional results suggest important differences in areas of intrinsic connectivity for the two groups.

The at-risk Alzheimer's disease data set is uniquely suited to this model. First, the smaller imaging acquisition area limits the number of regions of interest to consider. Secondly, the large number of subjects also allows for the estimation of a finer regional parcelation of the connectivity matrix. For example, if the study had typical group sizes of 15 or 20 per group, estimation of 46×46 covariance matrix would not be feasible, and hence regions would have to be aggregated to employ the model.

With regard to the model, its weakest point is the reliance on Gibbs-friendly priors for the variance components. In particular, the use of inverted gamma priors (with small rates and scales) and the inverse Wishart distribution for the variance components has been widely discussed and criticized (Daniels, 1999; Daniels and Kass, 1999; Daniels and Pourahmadi, 2002; He and Hodges, 2008; Yang and Berger, 1994). The previous references provide several alternative priors and approaches, including placing the priors on the eigenspace rather than the natural units. Such approaches are appealing in this setting, because principal component analysis of the region-specific random effects is of interest. However, a very practical solution would simply use a mixture of two or three gammas for the precisions and a mixture of two or three Wishart distributions for the inverse variance matrices. These solutions may add enough hyperparameters to allow for needed flexibility for the prior distributions, while still retaining a simple structure.

We discuss possible methods for further computational acceleration, though, as previously mentioned, the chain ran adequately fast for our application. However, for whole

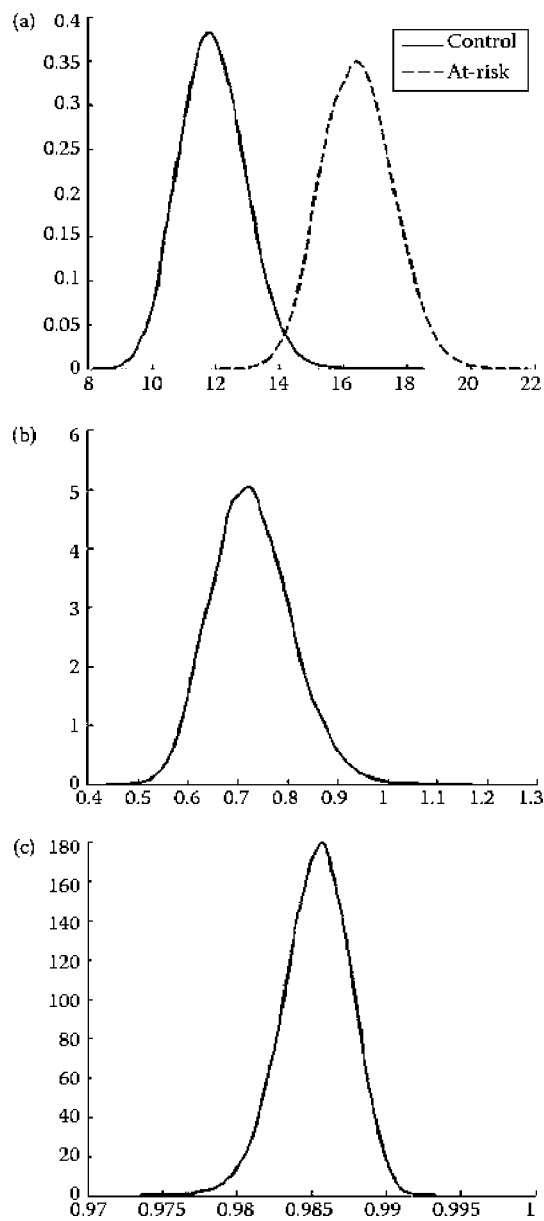


FIGURE 14.11
(a) Density estimates for the posterior distribution of the largest eigenvalue for R_i for the control (solid) and at-risk (dashed) groups. (b) Density estimates for the posterior distribution of the ratio of the largest eigenvalues for R_1 divided by that of R_2 . (c) Density estimate for the posterior distribution for the greatest root statistic.

brain results and next generation scanners, the extent of the computations will increase dramatically. A possible acceleration could be obtained with parallel processing. To be specific, the region- and group-specific parameters, μ_{gj} , σ_{gj} and λ_{gj} , are all conditionally independent given the inter-regional parameters, α_{ij} and Γ_j . Hence, they could be updated in parallel, hopefully speeding up calculations by an order of magnitude. We have

successfully applied this approach in unrelated areas with good success, though it was not applied here.

Perhaps the greatest challenge in this setting, and most germane to the topic of this book, is the question of the overall validity of the use of MCMC as a mechanism for analysis. While our application possessed only tens of thousands of parameters, current MRI and genomic technology puts the relevant number closer to millions. To our knowledge, convergence, implementation, diagnostic, and inferential issues for such large chains have had little discussion in the MCMC literature and represent a great challenge for future MCMC research.

References

- Arfanakis, K., Cordes, D., Haughton, V., Moritz, C., Quigley, M., and Meyerand, M. 2000. Combining independent component analysis and correlation analysis to probe interregional connectivity in fMRI task activation datasets. *Magnetic Resonance Imaging*, 18(8):921–930.
- Bassett, S., Yousem, D., Cristinzio, C., Kusevic, I., Yassa, M., Caffo, B., and Zeger, S. 2006. Familial risk for Alzheimer's disease alters fMRI activation patterns. *Brain*, 129(5):1229.
- Beckmann, C., Jenkinson, M., and Smith, S. 2003. General multilevel linear modeling for group analysis in fMRI. *NeuroImage*, 20(2):1052–1063.
- Biswal, B., Yetkin, F., Haughton, V., and Hyde, J. 1995. Functional connectivity in the motor cortex of resting human brain using echo-planar MRI. *Magnetic Resonance Medicine*, 34(4):537–541.
- Bookheimer, S., Strojwas, M., Cohen, M., Saunders, A., Pericak-Vance, M., Mazziotta, J., and Small, G. 2000. Patterns of brain activation in people at risk for Alzheimer's disease. *New England Journal of Medicine*, 343:450–456.
- Bowman, F., Caffo, B., Bassett, S., and Kilts, C. 2008. A Bayesian hierarchical framework for spatial modeling of fMRI data. *NeuroImage*, 39(1):146–156.
- Bowman, F. and Kilts, C. 2003. Modeling intra-subject correlation among repeated scans in positron emission tomography (PET) neuroimaging data. *Human Brain Mapping*, 20:59–70.
- Brookmeyer, R., Gray, S., and Kawas, C. 1998. Projections of Alzheimer's disease in the United States and the public health impact of delaying disease onset. *American Journal of Public Health*, 88:1337–1342.
- Calhoun, V., Adali, T., Hansen, L., Larsen, J., and Pekar, J. 2003. ICA of functional MRI data: An overview. *Fourth International Symposium on Independent Component Analysis and Blind Source Separation*, pp. 281–288.
- Cao, J. and Worsley, K. 2001. Applications of random fields in human brain mapping. *Spatial Statistics: Methodological Aspects and Applications*, 159:170–182.
- Daniels, M. 1999. A prior for the variance in hierarchical models. *Canadian Journal of Statistics*, 27(3):567–578.
- Daniels, M. and Kass, R. 1999. Nonconjugate Bayesian estimation of covariance matrices and its use in hierarchical models. *Journal of the American Statistical Association*, 94(448):1254–1263.
- Daniels, M. and Pourahmadi, M. 2002. Bayesian analysis of covariance matrices and dynamic models for longitudinal data. *Biometrika*, 89(3):553–566.
- Fox, N., Crum, W., Seahill, R., Stevens, J., Janssen, J., and Rossor, M. 2001. Imaging of onset and progression of Alzheimer's disease with voxel-compression mapping of serial magnetic resonance images. *Lancet*, 358(9277):201–205.
- Frackowiak, R., Friston, K., Firth, C., Dolan, R., Price, C., Zeki, S., Ashburner, J., and Penny, W. (eds) 2004. *Human Brain Function*, 2nd edn. Elsevier Academic Press, Amsterdam.
- Friston, K., Ashburner, J., Stefan, K., Nichols, T., and Penny, W. (eds) 2007. *Statistical Parametric Mapping: The Analysis of Functional Brain Images*. Elsevier Academic Press, Amsterdam.

- Friston, K., Glaser, D., Henson, R., Kiebel, S., Phillips, C., and Ashburner, J. 2002. Classical and Bayesian inference in neuroimaging: Applications. *NeuroImage*, 16:484–512.
- Friston, K., Holmes, A., Price, C., Büchel, C., and Worsley, K. 1999. Multisubject fMRI studies and conjunction analyses. *NeuroImage*, 10(4):385–396.
- Friston, K., Holmes, A., Worsley, K., Poline, J., Frith, C., Frackowiak, R. et al. 1995. Statistical parametric maps in functional imaging: A general linear approach. *Human Brain Mapping*, 2(4):189–210.
- Friston, K., Penny, W., Phillips, C., Kiebel, S., Hinton, G., and Ashburner, J. 2002. Classical and Bayesian inference in neuroimaging: Theory. *NeuroImage*, 16(2):465–483.
- Friston, K., Stephan, K., Lund, T., Morcom, A., and Kiebel, S. 2005. Mixed-effects and fMRI studies. *NeuroImage*, 24(1):244–252.
- Friston, K., Worsley, K., Frackowiak, R., Mazziotta, J., and Evans, A. 1993. Assessing the significance of focal activations using their spatial extent. *Human Brain Mapping*, 1(3):210–220.
- Gazzaniga, M., Ivry, R., and Mangun, G. 2002. *Cognitive Neuroscience: The Biology of the Mind*, 2nd edn. Norton, New York.
- Greicius, M. 2003. Functional connectivity in the resting brain: A network analysis of the default mode hypothesis. *Proceedings of the National Academy of Sciences of the USA*, 100(1): 253–258.
- Greicius, M. 2004. Default-mode network activity distinguishes Alzheimer's disease from healthy aging: Evidence from functional MRI. *Proceedings of the National Academy of Sciences of the USA*, 101(13):4637–4642.
- Hayasaka, S. and Nichols, T. 2003. Validating cluster size inference: Random field and permutation methods. *NeuroImage*, 20(4):2343–2356.
- He, Y. and Hodges, J. 2008. Point estimates for variance-structure parameters in Bayesian analysis of hierarchical models. *Computational Statistics and Data Analysis*, 52:2560–2577.
- Holmes, A. and Friston, K. 1998. Generalisability, random effects and population inference. *NeuroImage*, 7(4):754.
- Jones, G., Haran, M., Caffo, B., and Neath, R. 2006. Fixed-width output analysis for Markov chain Monte Carlo. *Journal of the American Statistical Association*, 101:1537–1547.
- MacEachern, S. and Berliner, L. 1994. Subsampling the Gibbs sampler. *American Statistician*, 48:188–190.
- Mardia, K., Kent, J., and Bibby, J. 1979. *Multivariate Analysis*. Academic Press, San Diego.
- Martin, A., Brouwers, P., Cox, C., and Fedio, P. 1985. On the nature of the verbal memory deficit in Alzheimer's disease. *Brain and Language*, 25(2):323–341.
- Nichols, T. and Holmes, A. 2002. Nonparametric permutation tests for functional neuroimaging: A primer with examples. *Human Brain Mapping*, 15(1):1–25.
- Ogawa, S., Lee, T., Kay, A., and Tank, D. 1990. Brain magnetic resonance imaging with contrast dependent on blood oxygenation. *Proceedings of the National Academy of Sciences of the USA*, 87(24):9868–9872.
- Roy, C. and Sherrington, C. 1890. On the regulation of the blood supply of the brain. *Journal of Physiology*, 11(85):108.
- Suckling, J. and Bullmore, E. 2004. Permutation tests for factorially designed neuroimaging experiments. *Human Brain Mapping*, 22(3):193–205.
- Tzourio-Mazoyer, N., Landeau, B., Papathanassiou, D., Crivello, F., Etard, O., Delcroix, N., Mazoyer, B., and M. J. 2002. Automated anatomical labeling of activations in SPM using a macroscopic anatomical parcellation of the MNI MRI single-subject brain. *NeuroImage*, 15:273–289.
- Verbeke, G. and Molenberghs, G. 2000. *Linear Mixed Models for Longitudinal Data*. Springer, New York.
- Woolrich, M., Behrens, T., Beckmann, C., Jenkinson, M., and Smith, S. 2004. Multilevel linear modelling for fMRI group analysis using Bayesian inference. *NeuroImage*, 21(4):1732–1747.
- Worsley, K. 1994. Local maxima and the expected Euler characteristic of excursion sets of χ^2 , F and t fields. *Advances in Applied Probability*, 26(1):13–42.
- Worsley, K. and Friston, K. 1995. Analysis of fMRI time-series revisited, again. *NeuroImage*, 2(3):173–181.

- Worsley, K., Liao, C., Aston, J., Petre, V., Duncan, G., Morales, F., and Evans, A. 2002. A general statistical analysis for fMRI data. *NeuroImage*, 15(1):1–15.
- Worsley, K., Marrett, S., Neelin, P., Vandal, A., Friston, K., and Evans, A. 1996. A unified statistical approach for determining significant signals in images of cerebral activation. *Human Brain Mapping*, 458:73.
- Xiong, J., Parsons, L., Gao, J., and Fox, P. 1999. Interregional connectivity to primary motor cortex revealed using MRI resting state images. *Human Brain Mapping*, 8(2–3):151–156.
- Yang, R. and Berger, J. 1994. Estimation of a covariance matrix using the reference prior. *Annals of Statistics*, 22(3):1195–1211.

